Total Oxidation of Naphthalene with Zirconia-Supported Cobalt, Copper and Nickel Catalysts

María S. Leguizamón Aparicio [1], Marco A. Ocsachoque [1], Delia Gazzoli [2], Irma L. Botto [3] and Ileana D. Lick [1,*]

[1] CINDECA (CCT La Plata- CONICET-UNLP), Departamento de Química, Facultad de Ciencias Exactas, Universidad Nacional de La Plata, Calle 47, N° 257, La Plata, Buenos Aires 1900, Argentina; mariasilvialap@quimica.unlp.edu.ar (M.S.L.A.); ocmarco@quimica.unlp.edu.ar (M.A.O.)

[2] Dipartimento di Chimica, Sapienza Universitá di Roma, 00185 Roma, Italy; delia.gazzoli@uniroma1.it

[3] CEQUINOR (CCT La Plata- CONICET-UNLP), Departamento de Química, Facultad de Ciencias Exactas, Universidad Nacional de La Plata, Bv. 120, N° 1465, La Plata, Buenos Aires 1900, Argentina; botto@quimica.unlp.edu.ar

* Correspondence: ilick@quimica.unlp.edu.ar; Tel.: +54-221-4211353

Abstract: $ZrO_2 \cdot nH_2O$ (hydrogel) impregnated with transition metals (Cu, Co, and Ni) was studied in this work as a precursor for the synthesis of CuO/ZrO_2 (CuZ), CoO_x/ZrO_2 (CoZ), and NiO/ZrO_2 (NiZ) catalysts, employed in the naphthalene oxidation reaction. Fresh and catalytically used materials were characterized by different physicochemical techniques, to compare the bulk and surface behavior, with particular attention to the effect of the supported metal species' properties on the catalytic activity. Techniques such as X-ray diffraction (XRD), temperature programmed reduction (TPR), differential scanning calorimetry (DSC), Brunauer–Emmett–Teller (BET) surface area analyzer, diffuse reflectance spectroscopy (DRS UV–vis), and Raman spectroscopy, allow for establishing structural and textural aspects of the support, as well as the surface coordination and the accessibility of supported species. Results were in agreement with the CuZ > CoZ > NiZ sequence for the activity in naphthalene oxidation reaction. Electronic properties, ionic sizes, oxide phase deposition on the support surface, reducibility, metal–support interaction, and local site symmetry of metals seem to be decisive factors for the catalytic interaction with the gaseous phase.

Keywords: combustion; hydrocarbons; Raman spectroscopies; naphthalene

1. Introduction

Volatile organic compounds (VOCs), emitted to the atmosphere by industrial and anthropic processes, are chemically associated to products derived from petrochemical processes and fuel combustion (e.g., automobile exhaust gas). They become hazardous for the environment, and particularly, for the human health.

Several processes, such as adsorption, thermal or catalytic oxidation, have been applied for the conversion of VOCs. Catalytic oxidation to carbon dioxide and water is one of the most promising methods for removing VOCs to carbon dioxide and water, since this process occurs at temperatures lower than those adopted by other non-catalytic processes, and can be used for effluent streams containing low VOC concentration [1–8].

Supported noble metal systems (Pt, Pd, Au, Rh) are recognized as the most active catalysts. However, the high cost of these metals and the easy of deactivation by sintering or poisoning limit industrial application [9].

Non-noble metal oxides catalysts (mainly Cu, Co, Ce, Mn, Cr, Fe) as simple, mixed or supported systems, are widely investigated for the oxidation of VOCs, due to many advantages, such as their low cost, low temperature activity, long lifetime, and regeneration capability, among others [10–15]. Interestingly, mixed oxide systems and supported systems perform better than the single oxide. This behavior is attributed to the high dispersion of the active phase, metal-support interaction, and to the increase of catalysts' reducibility, which are critical parameters for VOC oxidation activity [16–18].

ZrO_2 is a promising support [19–22] as well as an active phase [23,24] in oxidation catalysis, because of its high thermal stability, specific surface area and acid-base properties. In addition, the phase composition and physicochemical properties of ZrO_2 strongly depend on precursors, preparation methods and conditions. As a support, zirconia can be stabilized in the tetragonal form within temperature range 500–900 °C by addition of foreign species, yielding to variations in the availability of active sites for the catalytic reaction, according to their local symmetries [25,26]. On the other hand, the ability of the zirconia lattice to incorporate bi- and tri-valent cations, generates defective solid solutions with oxygen vacancies. In this sense, it is known that the number of bulk and sub-surface defects influences the properties and activity of materials, as it facilitates the migration of oxygen species from bulk to surface.

Although catalytic total oxidations of VOCs have been widely investigated, the investigation in specific types of VOCs, such as polycyclic aromatic hydrocarbons (PAHs), is much lower. PAHs are mainly released by combustion processes [8], and have been identified as carcinogenic pollutants. Naphthalene is, among them, the most volatile one, therefore, efforts have to be made to reduce its ecotoxicological impact. A few studies have tested the catalytic oxidation of naphthalene using both noble metals [27–29] and non-noble metal based catalysts, investigating the role of both the supported species and the support. As for non-noble metal active phase systems, including MnO_x, Co_3O_4, Fe_2O_3, CuO, TiO_2, and CeO_2, the catalytic performances were found to depend not only on redox properties, but also, on the interaction between reactant molecules and catalyst surface [18,30,31].

The aim of this work is the development of CuZ, CoZ, and NiZ systems, obtained by the impregnation of $ZrO_2 \cdot nH_2O$ (hydrogel hydrous zirconium oxide) with Cu-, Co-, and Ni-transition metal solutions, to be employed in the catalytic naphthalene oxidation reaction.

BET surface area, SEM-EDS, XRD, DSC, DRS-UV–vis, and TPR, among others, gave bulk information, whereas the Raman spectroscopy allowed the knowledge of the molecular behavior of species at surface level, where volatile organic compounds, oxygen, metal oxide and support can be simultaneously interacting. The physicochemical characterization of fresh and thermally treated materials, was related to the activity of each system, focusing on the comparative behavior related to the symmetry, coordination, and reduction of metal species on the support, and on the structural variation of the support caused by thermal treatments, as well as by the presence of added species.

2. Results and Discussion

Table 1 collects data for both the support and the supported samples corresponding to specific surface area, transition metal (TM) to zirconium atomic ratios obtained by the semiquantitative surface analysis by energy dispersive X-ray spectroscopy and the transition metal/Zr nominal ratio, structural type of metal oxide or stabilized zirconia polymorphic phase, as well as the reduction capability (expressed as H_2 consumed), as will be discussed later. For all the catalysts, surface ratios (EDS) are greater than nominal ratios, suggesting that metallic species are mostly present on the surface of the support. The increase in the time of the thermal treatment generates an increase in the surface ratio TM/Zr. The CoZ 5 h catalyst is the sample that show higher TM surface content.

Thermal treatments and the presence of foreign species affected some support properties, including phase transition and sintering. The contraction of the specific surface area can be associated to the thermal treatment and to the interaction with the supported species; however, the heating time seems not to be a decisive factor for specific surface area modifications.

Table 1. Specific surface area, EDS results, and crystalline phases of the samples.

Samples	S_{BET} (m$^2 \cdot$g^{-1})	Nominal TM/Zr *	EDS TM/Zr	Phases **	H$_2$ Consumed (mmoles)
ZrO$_2 \cdot n$H$_2$O	340	-	-	A	-
ZrO$_2$ 2 h	50	-	-	M	-
ZrO$_2$ 5 h	48	-	-	M	-
CoZ 2 h	37	0.110	0.362	T, Co$_3$O$_4$	0.029
CuZ 2 h	52	0.102	0.331	T	0.021
NiZ 2 h	29	0.111	0.266	M	0.019
CoZ 5 h	38	0.110	0.549	T, Co$_3$O$_4$	0.031
CuZ 5 h	56	0.102	0.398	T	0.023
NiZ 5 h	26	0.111	0.334	T, M (traces), NiO	0.020

* MT: Transition Metal; ** A = Amorphous; M = Monoclinic; T = Tetragonal.

XRD patterns of undoped ZrO$_2$(Z) and fresh NiZ catalysts heated for 2 h showed the ZrO$_2$ monoclinic phase (reflections located at 28.2°, 31.5°, 34.2°, and 50.2° of 2θ, PDF N° 03-065-1025), whereas the metastable tetragonal phase (reflections located at 30.0°, 35.0°, and 50.0° of 2θ, PDF N° 01-089-7710) was identified for the CoZ and CuZ samples (Figure 1A). The calcination for 5 h in air did not modify the structural properties of CoZ and CuZ samples. On the contrary, for NiZ system, the prolonged thermal treatment favored the formation of the metastable tetragonal phase.

As well documented in the literature [32–35], the interaction between the supported species and a support surface from the hydrous state yields changes in support properties and in supported species. During thermal treatment, adsorbed species interacting with the support surface hinder crystallization and sintering processes favoring the dispersion of active species.

Depending on the interaction strength, supported species may end up as dispersed or separate phase (crystalline or amorphous) or dissolved in the support to give a solid solution [32].

The effect of Cu, Co, and Ni on zirconia crystallization process was different, prevailing the metastable tetragonal form in CuZ and CoZ systems, and the monoclinic one in NiZ for short calcination time. The kinetically dependent process observed for NiZ system suggests that the interaction between zirconia and Ni(II) species is not only confined to the surface, but also involves incorporation into the zirconia structure [35].

No appreciable changes were detected in the XRD patterns of CoZ and CuZ samples (thermal treatments for 2 h or 5 h) after catalytic tests. On the contrary, for the NiZ system, a strong contribution of the metastable tetragonal phase was already detected in the NiZ 2 h sample after catalytic runs, confirming the kinetic contribution to the interaction process (Figure 1B).

In addition to zirconia modifications, reflections due to NiO and Co$_3$O$_4$ spinel structure (typical lines located at 37.3°, 43.3°, 62.9°, 87.0° of 2θ, PDF N° 03-065-6920 [36,37] and at 36.8°, 31.2°, 44.7°, 65.1° and 59.3° of 2θ, PDF N° 01-080-1533 [38–40] respectively),were detected for NiZ and CoZ samples after thermal treatment for 5 h.

Likewise, no diffraction lines due to CuO (located 38.8°, 35.5°, 39.0° and 48.7° of 2θ, PDF N° 01-080-1917) were observed in CuZ patterns. This finding can be attributed to the presence of CuO species with crystal size smaller than the XRD detection capacity or to copper incorporation in the zirconia lattice, as already observed [41,42].

Raman spectroscopy was used to determine the structure of the added species and of the zirconia support [43], both in amorphous and crystalline form, as well as the structure adopted by the metal-O species, either supported or interacting. In fact, this spectroscopic technique is highly sensitive to oxygen displacement, owing to its high polarizability and to intermediate range order without long-range periodicity [44].

According to group factor analysis, distinct and characteristic bands in the 100–650 cm^{-1} range are predicted for the monoclinic (18 Raman active modes) and tetragonal (6 Raman active modes) ZrO$_2$ modifications. In particular, over the range 100–300 cm^{-1}, the monoclinic phase has two bands at 179

and 191 cm^{-1}, well separated from the tetragonal bands appearing at 147 and 261 cm^{-1}. This evidence allows distinguishing different structures in mixed tetragonal/monoclinic zirconia phases.


(A)

(B)
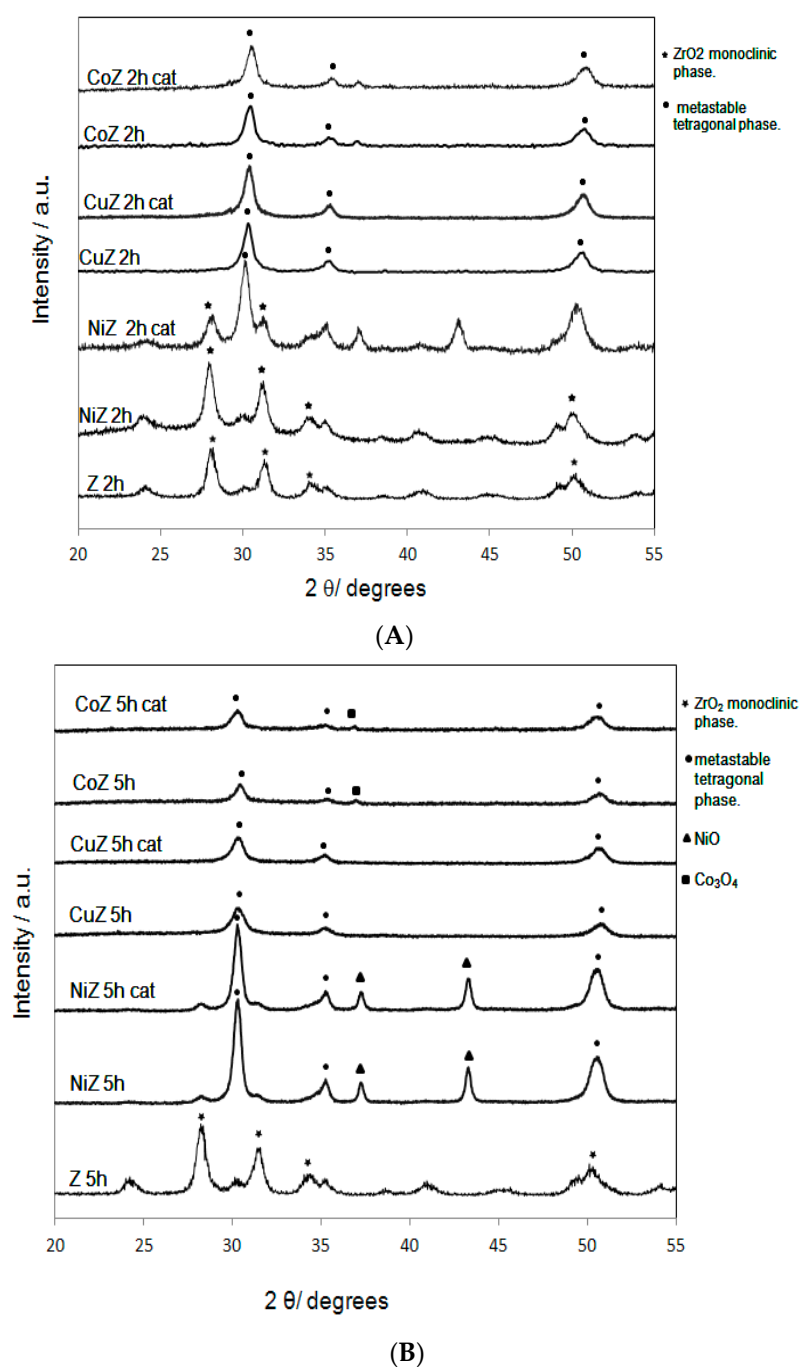
Figure 1. (**A**) XRD patterns of fresh and used catalysts calcinated for 2 h. (**B**) XRD patterns of fresh and used catalysts calcinated for 5 h.

The most representative Raman spectra of investigated systems, together with those of monoclinic and tetragonal ZrO$_2$, are illustrated in Figures 2–4. Spectral analysis of CoZ samples before and after the catalytic test, Figure 2, revealed the features of both the monoclinic and tetragonal phases (curves (a), (b) and (c)) in all samples, with tetragonal components becoming predominant, increasing the duration of the heat treatment (curve (b)). No significant changes were induced by the catalytic runs. Curve d identifies the presence of Co$_3$O$_4$ nanocrystals randomly distributed in all the CoZ materials.

For Co_3O_4 spinel structure (Co^{2+} located at the tetrahedral site (Td) and Co^{3+} at the octahedral one (Oh)), Raman peaks are predicted to appear at 194 cm^{-1} (F2g), 485 cm^{-1} (Eg), 523 cm^{-1} (F2g), 620 cm^{-1} (F2g, Td site), and at 693 cm^{-1} (A1g; Oh site) [45].

The CoO presence would contribute with a Raman signal that was relatively weak and superimposed to those of Co_3O_4 [46].
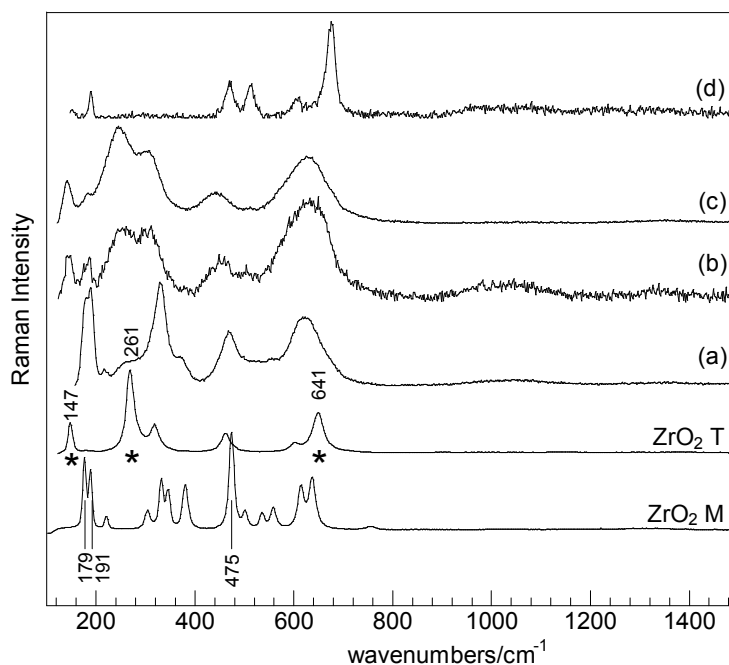
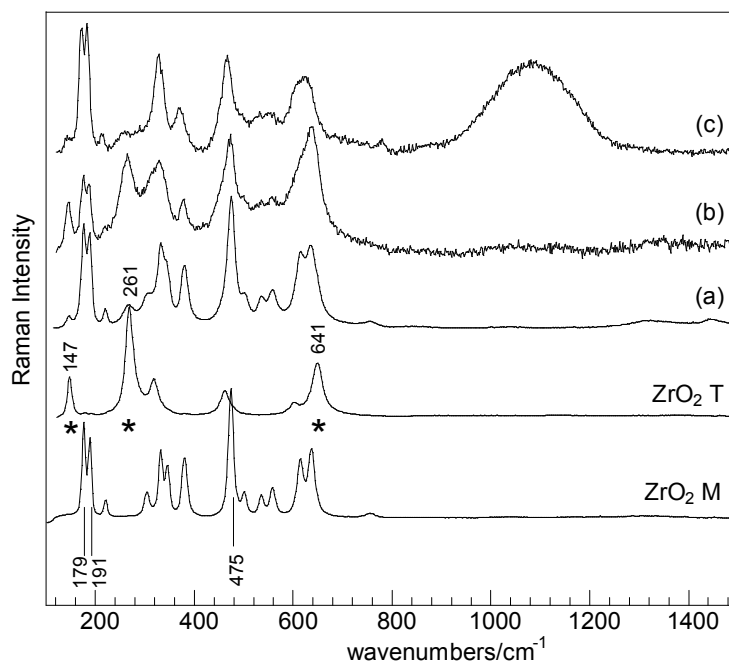**Figure 2.** Raman spectra of CoZ samples after different treatments: (**a**) 600 °C 2 h; (**b**) 600 °C 5 h; (**c**) after catalytic test; (**d**) Co_3O_4 nanocrystals randomly distributed in all samples. The asterisks indicate the position of the main bands of the tetragonal phase (ZrO_2 T), and the vertical bars the position of the main bands of the monoclinic phase (ZrO_2 M).

Figure 3 shows the most representative Raman spectra of NiZ system before and after catalytic investigation. The spectrum of thermally treated sample (curve (a)) consisted mainly of bands due to the monoclinic phase, and showed some weak feature of the tetragonal phase (Figure 3, curve (a)). After catalytic runs, features of both tetragonal and monoclinic modifications (curve (b)) were revealed, and in addition, a band at about 1080 cm^{-1}, characteristic of nanosized NiO (curve (c)), was also detected.

For single-crystal or polycrystalline NiO, vibrational bands are predicted at about 420 and 560 cm^{-1} due to one-phonon (1P) (TO and LO modes), at about 730 cm^{-1} due to two-phonon (2P) (2TO modes), at about 906 cm^{-1} (TO + LO), and 1090 cm^{-1} (2LO modes) [47,48]. Furthermore, the intensities of the (1P) band (about 560 cm^{-1}) and that of (2P) band (about 1100 cm^{-1}) strongly depend on NiO particle sizes and on their defectivity; the smaller the size the higher the intensity and defectivity. Although the band at 560 cm^{-1} is obscured by ZrO_2 bands, the strong feature at about 1080 cm^{-1} is a clear indication of nanosized NiO presence.

The Raman spectrum collected on the CuZ sample after 2 h heating contains mainly the bands due to monoclinic phase, and small contributions because of tetragonal phase, Figure 4, curve (a). After treatment at 600 °C 5 h and after catalytic test with $C_{10}H_8$, bands due to tetragonal ZrO_2 (Figure 4, curve (b) and (c)) were recorded. No evidence of CuO separate phase could be found by Raman analysis. Because three active modes at 298, 345, and 632 cm^{-1} are predicted for CuO [49], the CuO presence should be evidenced by a band resulting from the overlapping of its most intense band (298 cm^{-1}), and the one at about 270 cm^{-1} of the ZrO_2 tetragonal phase.

Figure 3. Raman spectra of NiZ samples after different treatments: (**a**) 600 °C 2 h; (**b**) 600 °C 5 h; (**c**) after catalytic test. The asterisks indicate the position of the main bands of the tetragonal phase (ZrO$_2$ T) and the vertical bars the position of the main bands of the monoclinic phase (ZrO$_2$ M).
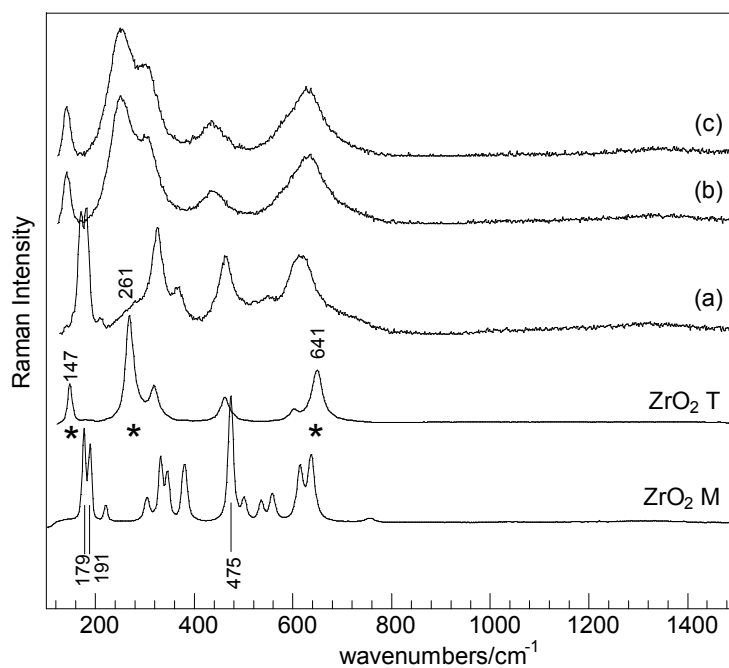
Figure 4. Raman spectra of CuZ samples after different treatments: (**a**) 600 °C 2 h; (**b**) 600 °C 5 h; (**c**) after catalytic test. The asterisks indicate the position of the main bands of the tetragonal phase (ZrO$_2$ T) and the vertical bars the position of the main bands of the monoclinic phase (ZrO$_2$ M).

Comparison of the Raman spectra among catalysts with those of monoclinic and tetragonal ZrO$_2$ support indicates a local order decrease in the supported systems that broaden the Raman bands. Because Raman scattering comes both from the surface and the bulk of samples, the band broadening indicates that ZrO$_2$ phase transition starts at the surface region. Differences between results from

Raman spectroscopy and XRD analysis can also be seen for almost all samples. For CoZ and NiZ systems and for CuZ 2 h sample, both tetragonal and monoclinic ZrO_2 phases were detected, whereas XRD results show the presence of tetragonal ZrO_2. These findings suggest, under our experimental conditions, that catalysts are heterogeneous materials.

Transformations occurring during calcination of hydrous zirconia, $ZrO_2 \cdot nH_2O$, as well as of catalytic precursors (M(II)/$ZrO_2 \cdot nH_2O$ (M(II) = Co, Cu and Ni), were studied using differential scanning calorimetry (DSC). Figure 5 reveals that the process occurs in two steps. The first one is characterized by a broad endothermic zone between 40 and 300 °C. Signals evolved by the broadband correspond to the removal of weakly bound water and to the decomposition of residual metal nitrate, used as impregnating agents. The second one is characterized by exothermic signals between 300 and 600 °C attributed to zirconia crystallization process. From DSC curves of Figure 5, it can be clearly observed that metal cations delay the crystallization process. The undoped zirconia presents two exothermic signals, the first one at 380 °C is associated to the oxolation of hydroxyl groups to form embryonic oxide nuclei and the second one at 420 °C is associated to the crystal growth process [50]. The introduction of metal ions reduces the amplitude of exothermic peaks and shifts them to a higher temperature. It is evident that the dopant presence retards significantly the processes as well documented in the literature [51,52]. The crystallization process is complex, and involves an arrangement which is different from the kinetic point of view than that observed in undoped zirconia. There must be a small degree of substitution of the Zr^{4+} ions for ions of lower charge (Cu^{2+}, Co^{3+}, Co^{2+} or Ni^{2+}) [21], a process that can be favored for similar ionic radii and higher surface areas. In addition, the host metals preferential coordination must be taken into account. Table 2 shows Shannon–Prewitt ionic radii values of studied species [53]. The formation of the oxygen-defective structure increases the mobility of oxygen atoms [54,55]. In fact, as observed by Raman spectroscopy, the tetragonal phase increases at surface level with the calcination time.
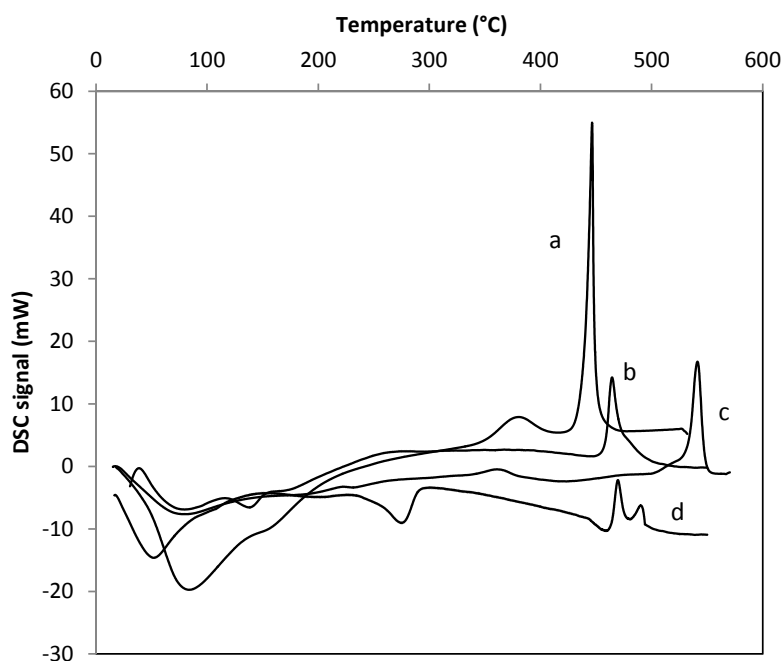
Figure 5. DSC diagrams of catalytic precursors. (**a**) Z; (**b**) CoZ; (**c**) CuZ; (**d**) NiZ.

It is well known that Zr(IV) in tetragonal phase presents octahedral coordination. This structural form is stabilized by the presence of bi and tri-valent host ions. In this context, Cu(II) ionic radius in octahedral environment is similar to that of Zr(IV) in similar coordination, although according to the electronic configuration, Cu(II) is more susceptible to adopting a distorted octahedral or square

planar environment, due to the Jahn–Teller effect. This aspect implies that the tetragonal stabilization must be kinetically less favorable, requiring consequently higher energy.

Table 2. Shannon–Prewitt ionic radii values of studied species.

Ion	Coordination	Ionic Radius
Co^{2+}	6 (LS)	0.65
Co^{3+}	6 (LS)	0.54
Cu^{2+}	Square plane	0.57
	6	0.73
Ni^{2+}	6	0.69
Z^{4+}	6	0.72

In fact, comparing the exothermic peaks exhibited by the catalytic precursors, the amorphous—crystalline tetragonal transformation occurs at the highest temperature for CuZ system. Differences with respect to the other metal species are responsible for the higher temperature observed for the copper re-arrangement in the zirconia lattice. Likewise, there are limits in the incorporation of copper in zirconia networks; so, the Cu-O species, which are not incorporated, contain Cu(II) ions with axial distortion. In this context, the broad signal in the 600–800 nm range for the CuZ 2 h UV–vis diffuse reflectance spectrum (Supplementary Materials) corroborates the presence of this coordination out the zirconia lattice [56].

Temperature programmed reduction (TPR) analysis was used to study redox properties of catalysts. Figure 6 shows the evolution of H_2 consumption as a function of temperature for catalysts. Furthermore, the reduction peaks were integrated, and the values of H_2 consumed (mmol), given in Table 1, are in acceptable agreement with that expected by the supported phases concentration. In the studied temperature range, zirconia does not show an appreciable consumption of hydrogen, although it is known that it can be partially reduced at high temperature (about 800 °C).

As it is shown in the Figure 6, depending on the supported transition metal oxide, the catalysts present different reducibility. Moreover, signals for CoO or CuO supported oxides appear in a temperature range slightly shifted with respect to that observed for pure oxides (Supplementary Materials) [19,57–60]. So, the pure Co_3O_4 TPR profile is characterized by two reduction steps, assigned to Co(III)–Co(II) and Co(II)–Co° (with maximums at 324 and 397 °C respectively) [19], while the TPR profiles of CoZ 2 h and CoZ 5 h catalysts show a series of signals in the range 260–360 °C, which indicate the presence of diverse types of cobalt oxide species, or species with different interactions over the support. Crystalline Co_3O_4 is not detected in the CoZ 2 h catalyst by DRX, revealing that cobalt oxide is highly dispersed in the zirconia, as was detected by Raman.

It is interesting to observe that the CuO reductions in the CuZ 2 h and CuZ 5 h catalysts occur at about 160 °C below the temperature observed for the pure CuO (around of 360 °C) [58,59], revealing a high dispersion of copper species, in agreement with CuO phase absence in the XRD pattern and Raman spectroscopy results.

The small size of the Co_3O_4 or CuO particles and/or the interaction of transition metal species with the zirconia surface may explain their reduction at lower temperature [21,61–63]. This suggests that the support favors the surface dispersion of the oxide, increasing the reducibility. In this context, it is also interesting to note that CuZ 2 h and CuZ 5 h catalysts present higher surface areas and lower sintering. Centi et al. [64] have reported that the reducibility of copper species increases on ZrO_2, especially on tetragonal phase. These authors suggest that during the hydrous zirconia calcination to give anhydrous ZrO_2, the OH groups were responsible for the reduction of Zr^{4+} into Zr^{3+} ions, whereas the presence of a lower oxidation state of Zr generates an increase of anionic vacancies concentration. Similar behavior is expected by the isomorphous substitution of Zr(IV) by transition metals, revealing that the effect of the vacancies of the zirconia lattice affects the redox properties of

supported oxide species, increasing the reducibility, because these supported particles are in a more reducing environment.
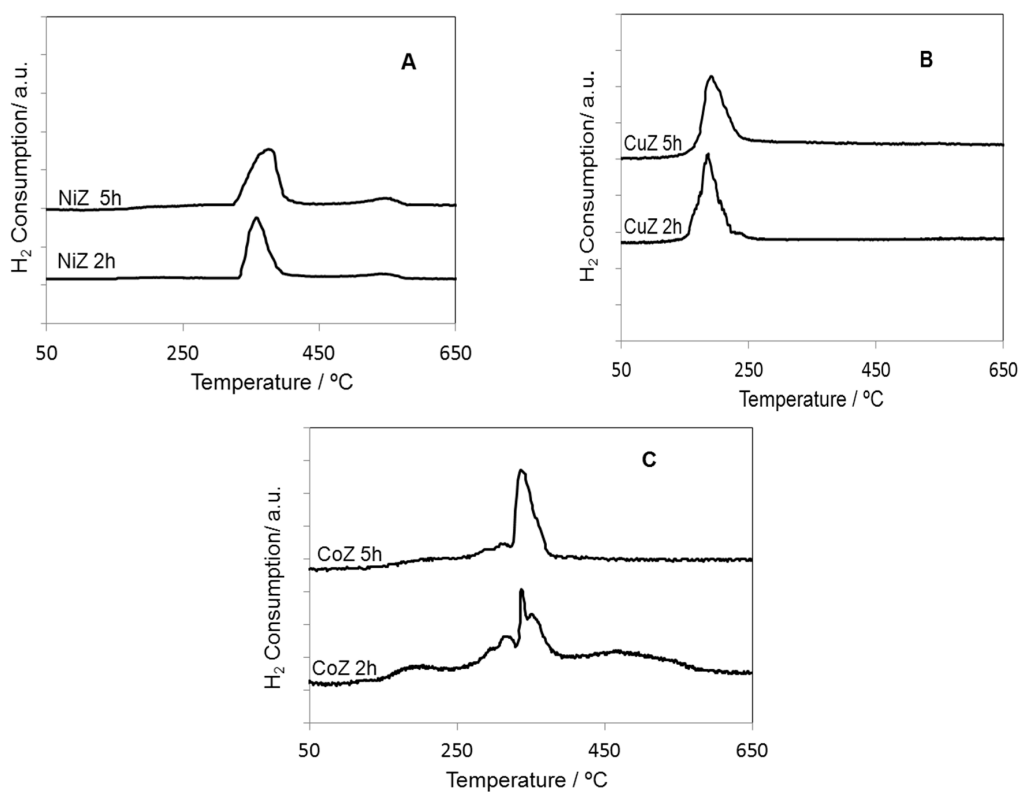
Figure 6. (**A**) NiZ, (**B**) CuZ and (**C**) CoZ. TPR patterns of fresh catalysts.

Finally, in contrast to that observed with the CoZ and CuZ catalysts, the presence of zirconia does not generate an increase in the reducibility of the supported NiO species. The pure NiO TPR profile shows H_2 consumption between 340 and 420 °C, while both NiZ 2 h and NiZ 5 h catalysts' TPR profiles show H_2 consumption in the same temperature range. It is possible to suggest a low interaction NiO-support in agreement with DRX and Raman results.

Likewise, the reduction of catalysts calcinated for 5 h occurs at temperatures slightly higher than those thermally treated during 2 h. This result can be attributed to a stronger metal-support interaction, and increase of diffusion by thermal effect (mobility of oxygen atoms), factors that improve the crystallization. Besides, it can be suggested a small crystal growth of oxide particles. In the case of the CoZ catalyst, these results are consistent with that observed in XRD, where the presence of Co_3O_4 crystals has been detected just in CoZ 5 h catalyst. Considering all the above, the reducibility of catalysts follows the order: CuZ 2 h > CuZ 5 h > CoZ 2 h > CoZ 5 h > NiZ 2 h > NiZ 5 h.

Catalytic activity results for the naphthalene oxidation reaction, expressed as CO_2 yield vs. temperature, are presented for all catalysts in Figure 7. Table 2 shows T50 and T90 values (temperature where conversions reached are 50% and 90%, respectively) obtained in each experiment. No CO or other by-products were observed in the outlet gas, and then, the selectivity towards CO_2 is higher than 99%.

When performing the experiment in catalyst absence, the T50 and T100 (temperature where conversions reached are 50% and 100%) are 430 °C and 485 °C, respectively. For the ZrO_2 support, a CO_2 yield of 50% is reached at 270–280 °C, obtaining the complete conversion (CO_2 yield of 100%) at 400 °C; it is evident that zirconia is active for naphthalene oxidation.

Transition metal oxide-modified catalysts show improved activities; with them, the total conversion of naphthalene is achieved at lower temperatures, in the range 220–300 °C. These results revealed that all catalysts were more active than the bare support. The relative order of catalyst

activity can be analyzed by comparing the required temperature to reach 50% of CO_2 yield (Table 3). By comparing the T50 values the activity of catalysts follows the order: CuZ 5 h > CuZ 2 h > CoZ 5 h > CoZ 2 h > NiZ 2 h ≈ NiZ5 h >> Z.
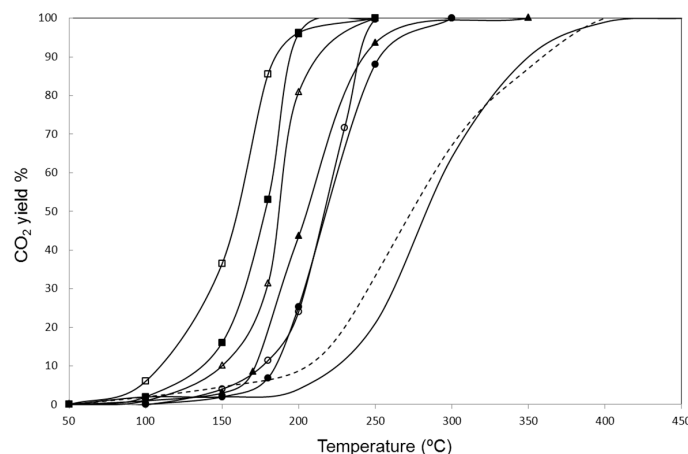
Figure 7. Catalytic activity in naphthalenecombustion: - - - Z 2 h; – Z 5 h; □ CuZ h; ■ CuZ 2 h; Δ CoZ 5 h; ▲ CoZ h; ○NiZ h; ●NiZ h.

Table 3. Comparison of naphthalene total oxidation activity for different catalysts.

Catalyst	T50 (°C)	T90 (°C)	GHSV (h^{-1})	Reference
Z 5 h	285	350	36,000	This work
Z 2 h	273	360	36,000	This work
CuZ 2 h	180	193	36,000	This work
CuZ 5 h	160	184	36,000	This work
CoZ 2 h	205	243	36,000	This work
CoZ 5 h	188	213	36,000	This work
NiZ 2 h	218	255	36,000	This work
NiZ 5 h	218	240	36,000	This work
Co_3O_4	245	270	60,000	[11]
0.12%Pt-Al_2O_3	204	310	20,000	[65]
Cu-Mn/Al_2O_3	207		20,000	[65]
$Ce_{0.75}Zr_{0.25}O_2$	290	320	-	[31]
Mn_2O_3	230	250	60,000	[13]
CeO_2	160	190	25,000	[30]
CeO_2-CuO			75,000	[66]
$CuMn_2O_4$	229	238		[18]
$CoO_x(15)$-SiO_2	228	260	18,000	[14]

On the other hand, the increase of the calcination time generates an increase in the activity of the catalysts, with this effect being more marked in CoZ and CuZ catalysts. This slight increase in activity may be associated with the higher surface content of the oxide transition metal species (Table 1). It may also be due to an increase in the concentration of oxygen vacancies. According to Raman spectroscopy, it has been observed that the CuZ 5 h catalyst has higher content of tetragonal phase on the catalytic surface than the CuZ 2 h catalyst.

The structural and redox behavior, as well as electronic properties of the different supported transition metal species, are expected to play a decisive role in the naphthalene oxidation, considering that the mechanism of hydrocarbons (HC) oxidation reaction (e.g., naphthalene) occurs through a redox process. One of the most used mechanisms to explain the catalytic oxidation of hydrocarbons is the Mars—van Krevelen mechanism, where active oxygen comes from catalytic oxide species [14,66]. In this context, Solsona et al. [67] carried out the propane oxidation process in oxygen absence using a CuO_x–CeO_2 catalyst, and detected oxygen containing compound (CO_2) as reaction product, suggesting the participation of lattice oxygen.

On the other hand, the Langmuir–Hinshelwood accepted mechanism proposes, as an important step of the process, the adsorption of the reactants in active sites. Labaki et al. [21] have studied the total oxidation of propene and toluene in the presence of zirconia doped by copper. These authors have proposed that the oxidation mechanism implies the intervention of chemisorbed activated oxygen. On zirconia, the adsorption of O_2 can be explained by the intervention of Zr^{3+}/Zr^{4+} redox cycles, the formation of $O_2^-{}_{ads}$, and anionic vacancies.

Taking into account the obtained results, both mechanisms may contribute to catalytic activity of catalyst in this work. Zirconia, with its oxygen vacancies, may be an oxygen adsorption site and may be a site of adsorption for the hydrocarbon.

Besides, in this work, catalysts that contain highly interacted transition metal oxides present greater activity than zirconia. It is possible to suggest an oxygen supply from the oxides to the reactants, following a Mars–van Krevelen MVK mechanism and generating a redox cycle. In this context, Co(III) can be reduced to Co(II), or Cu(II) to Cu(I). The presence of zirconia oxygen vacancies favors these processes because the reducibility of species increases, as was observed by TPR results. The high metal–support interaction generates a greater mobility of oxygen in the catalytic system, and this property can increase the activity. Moreover, the greater metal–zirconia interaction favors the formation of vacancies in the bulk, and consequently, facilitates the movement of oxygen in the catalytic system from the bulk to the surface. A similar effect has been reported for the $Cu–CeO_2$ system [67]. Finally, reduced sites should be re-oxidized to be regenerate.

From results, it is evident that the activity may also depend on the metal coordination of supported species. Hence, the less active catalyst (ZNi), containing d^8Ni(II) species in octahedral coordination, presents lower redox possibilities with respect to CoZ and CuZ catalysts.

In CoZ catalysts, cobalt oxide adopts the easily reducible spinel structure (Co(III) with low spin d^6 configuration and octahedral coordination, and Co(II) with d^7 configuration and tetrahedral coordination).

For the CuZ system, the lower copper symmetry, due to the Jahn–Teller effect, can explain the higher accessibility to the active site. CuZ catalysts shows the highest activity among the supported catalysts, because of their special copper–zirconia interaction, their high possibility of generated oxygen vacancies, their higher area, and their higher reducibility. CuO particles are nano-dispersed on catalytic surface, and have not been detected with the characterization techniques used (DRX and Raman spectroscopy).

It is interesting to remark that in all cases, the activity is enhanced with the time length of thermal treatment. This fact facilitates diffusion processes, allowing an adequate rearrangement of metal species, accompanied by the stabilization of zirconia tetragonal phase, increasing the oxygen vacancies, and leaving exposed, a higher number of active sites.

On the other hand, under our experimental conditions, no significant changes in the physicochemical properties of CuZ catalysts were induced by the catalytic runs.

Finally, considering the obtained and reported results (Table 3), it can be suggested that the CoZ, and, more specifically, the CuZ catalysts show an appreciable activity for the catalytic oxidation of naphthalene.

3. Experimental Section

3.1. Material Preparation

Hydrous zirconium oxide, $ZrO_2 \cdot nH_2O$, was prepared by precipitation from a $ZrOCl_2 \cdot 6H_2O$ (Fluka) solution with ammonium hydroxide (up to pH 10). The process was carried out at room temperature with constant stirring for 6 h. The pH was maintained close to 10. After filtration, the solid was washed (Cl^- negative test in the solid) and dried at 100 °C for 6 h. Portions of $ZrO_2 \cdot nH_2O$ were impregnated with an aqueous solution of M(II) nitrates (M(II) = Cu, Co, Ni), to obtain materials with a metal concentration of 5% *wt/wt* (expressed as grams of Cu, Co and Ni by 100 g of catalyst).

After drying, the samples were divided into two groups, and thermally treated at 600 °C for 2 h and 5 h, respectively.The obtained materials were named CoZx h, CuZx h, and NiZx h, where Z = zirconia, and xh stands for the length of heat treatment (h).

3.2. Catalyst Characterization

Catalyst surface areas were determined using the BET technique, and were performed using a Micromeritics Accusorb 2100 E instrument. Energy dispersive X-ray spectroscopy (EDS) analyses were performed using a SEM Philips 505 microscope provided with an EDAX DX PRIME 10 energy dispersive X-ray analyzer. Powder X-ray diffraction (XRD) patterns were recorded on an X-ray diffractometer (Philips PW 1732/10) with Cu Kα(Ni-filtered) radiation. Raman spectra of fresh and used catalysts were measured at room temperature in back-scattering geometry with an in Via Renishaw micro-Raman spectrometer equipped with an air-cooled CCD detector and edge filters. The emission line at 488.0 nm from an argon ion laser was focused on the sample under a Leica DLML microscope using 20$\times$ or 5$\times$ objectives, and the power of the incident beam was about 5 mW. Several (10 or 20 s) accumulations were acquired for each catalyst sample. The spectral resolution was 2 cm^{-1}, and spectra were calibrated using the 520.5 cm^{-1} line of a silicon wafer. Spectra processing included baseline removal and curve fitting using a Gauss–Lorentz cross product function by Peakfit 4.12 software (Jandel, AISN Software). Differential scanning calorimetry (DSC) diagrams of catalytic precursors were recorded with a DSC-50 Shimadzu instrument, using N$_2$ as inert gas flow, a heating rate of 10 °C min^{-1}, and a mass of 10 mg. Diffuse Reflectance UV–visible spectra (DRS-UV–vis) of CuZ catalysts were obtained with a Perkin Elmer Lambda 35 UV-VIS spectrometer. Temperature programmed reduction (TPR) analysis was performed in home-made equipment. The sample (30.0 mg) was placed in an electrically heated fixed-bed quartz micro-reactor, and heated from 50 to 800 °C with a heating rate of 10 °C/min. In experiments, 10% hydrogen in nitrogen (flow rate 20 mL min^{-1}) was used. Hydrogen consumption was detected by a thermal conductivity detector (TCD).

3.3. Catalytic Activity for Naphthalene Oxidation

Catalysts' performance was measured using an electrically heated fixed-bed quartz reactor (id = 0.8 cm) containing 0.100 g of catalyst, the temperature of the catalyst being monitored by a k-type thermocouple. A schematic diagram of the reaction system is shown in Figure 8.
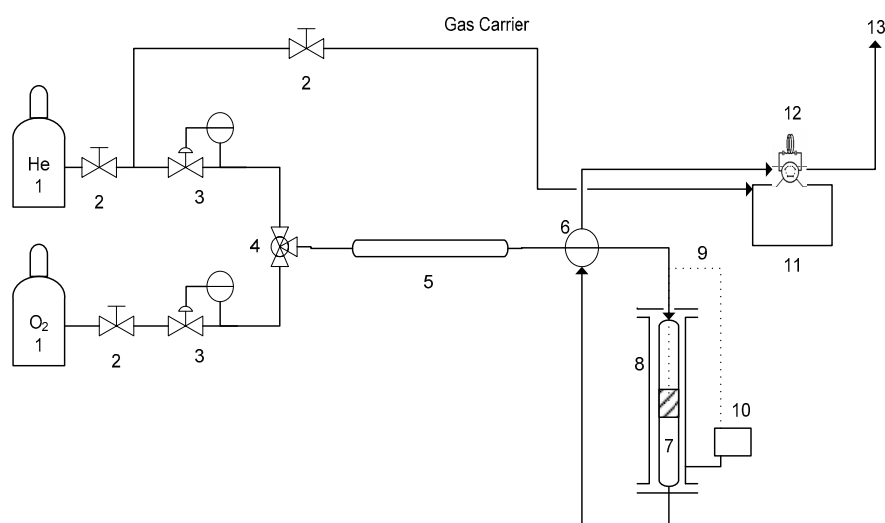
Figure 8. The experimental apparatus : (**1**) cylinders (He, O$_2$); (**2**) On–off valves; (**3**) mass flow controllers; (**4**) Tee valves; (**5**) vaporization of naphthalene; (**6**) four-way valve; (**7**) quartz reactor; (**8**) furnace; (**9**) thermocouple type k; (**10**) thermostat; (**11**) gas chromatography; (**12**) injection valve unit; (**13**) vent.

Reactions were carried out using a mixture of 10% oxygen and 90% helium, and 150 ppm naphthalene. The total flow rate was 30 mL/min. To achieve a stable concentration of naphthalene in the gas phase, the input current passes through a thermostated saturator containing this reactive. Despite this, the combustion experiment was initiated as soon as a stable vapor pressure was reached. As the system must reach the equilibrium for each reaction temperature, to ensure the result, several analyses were performed for each temperature. Products were analyzed by a Shimadzu gas chromatograph, model GC 2014, with a thermal conductivity detector. The total $C_{10}H_8$ conversion was calculated by the following equation:

$$XCO_2 \ = \ 1/10 \ [CO_2]/[C_{10}H_8] \tag{1}$$

where $[CO_2]$ is gas-phase concentration after reaction and $[C_{10}H_8]$ is feed concentration.

4. Conclusions

According to the results, all catalysts based on transition metal oxide supported on zirconia are active for total oxidation of naphthalene, increasing significantly, the activity of pure zirconia. Catalytic performance follows the CuZ > CoZ > NiZ >> ZrO_2 sequence. A set of factors determine the catalytic efficiency, such as surface area, crystallite size, the surface dispersion of metal oxide, similarity between Zr(IV) and metal ionic radii, number of vacancies generated by cationic substitution, mobility of oxygen vacancies from the bulk to sub-surface, local symmetry of metal, stabilization of zirconia tetragonal phase, and metal reducibility. Physicochemical techniques applied in this work reveal that CuZ is the best catalytic system, presenting a similar behavior to that reported in literature for the most active catalytic materials in the naphthalene oxidation. All these properties contribute to suggest the temporal Cu(II)–Cu(I) redox cycle, through the oxide defects, or to the low coordination of very reactive surface oxygen atoms in the CuO phase nano-dispersed on the zirconia. Although, it is also possible that the Co(III)–Co(II) redox cycle and lower activity of cobalt catalysts are attributed to the stabilization of surface spinel crystal phase, clearly detected by the techniques, whereas the high thermodynamic stability of NiO contributes to the formation of the crystal oxide on the zirconia surface, with a marked decrease of the required properties for the CO_2 production.

Author Contributions: I.L.B. and I.D.L. conceived and designed the experiments; M.S.L.A. and M.A.O. performed the experiments; D.G. contributed with Raman spectroscopy analysis and carefully revised the manuscript, all authors discussed results; I.D.L and I.L.B. wrote the manuscript. All authors read, revised and approved the final manuscript.

Conflicts of Interest: The authors declare no conflict of interest.

References

1. Demoulin, O.; Clef, B.L.; Navez, M.; Ruiz, P. Combustion of methane, ethane and propane and of mixtures of methane with ethane or propane on Pd/γ-Al_2O_3 catalysts. *Appl. Catal. A* **2008**, *344*, 1–9. [CrossRef]
2. Solsona, B.; Garcia, T.; Hutchings, G.J.; Taylor, S.H.; Makkee, M. TAP reactor study of the deep oxidation of propane using cobalt oxide and gold-containing cobalt oxide catalysts. *Appl. Catal. A* **2009**, *365*, 222–230. [CrossRef]
3. Onda, A.; Suzuki, Y.; Takemasa, S.; Kajiyosh, K.; Yanagisawa, K. Catalytic wet oxidations of aromatic compounds over supported copper oxides. *J. Mater. Sci.* **2008**, *43*, 4230–4235. [CrossRef]
4. Okal, J.; Zawadzki, M. Combustion of propane over novel zinc aluminate-supported ruthenium catalysts. *Appl. Catal. B Environ.* **2011**, *105*, 182–190. [CrossRef]

5. Ntainjua, E.N.; Davies, T.E.; García, T.; Solsona, B.; Taylor, S.H. The Influence of Platinum Addition on Nano-Crystalline Ceria. Catalysts for the Total Oxidation of Naphthalene a Model Polycyclic Aromatic Hydrocarbon. *Catal. Lett.* **2011**, *14*, 1732–1738. [CrossRef]

6. Baranowska, K.; Okal, J. Bimetallic Ru-Re/γ-Al$_2$O$_3$ catalysts for the catalytic combustion of propane: Effect of the Re addition. *Appl. Catal. A* **2015**, *499*, 158–167. [CrossRef]

7. García, T.; Agouram, S.; Taylor, S.H.; Morgan, D.; Dejoz, A.; Vázquez, I.; Solsona, B. Total oxidation of propane in vanadia-promoted platinum-alumina catalysts: Influence of the order of impregnation. *Catal. Today* **2015**, *254*, 12–20. [CrossRef]

8. Kamal, M.S.; Razzak, S.A.; Hossain, M.M. Catalytic oxidation of volatile organic compounds (VOCs)—A review. *Atmos. Environ.* **2016**, *140*, 117–134. [CrossRef]

9. Liotta, L.F. Catalytic oxidation of volatile organic compounds on supported noble metals. *Appl. Catal. B Environ.* **2010**, *100*, 403–412. [CrossRef]

10. Ataloglou, T.; Vakros, J.; Bourikas, K.; Fountzoula, C.; Kordulis, C.; Lycourghiotis, A. Influence of the preparation method on the structure–activity of cobalt oxide catalysts supported on alumina for complete benzene oxidation. *Appl. Catal. B Environ.* **2005**, *57*, 299–312. [CrossRef]

11. García, T.; Solsona, B.; Taylor, S.H. Naphthalene total oxidation over metal oxide catalysts. *Appl. Catal. B Environ.* **2006**, *66*, 92–99. [CrossRef]

12. Aranda, A.; López, J.M.; Murillo, R.; Mastral, A.M.; Dejoz, A.; Vázquez, I.; Solsona, B.; Taylor, S.H.; García, T. Total oxidation of naphthalene with high selectivity using a ceria catalyst prepared by a combustion method employing ethyleneglicol. *J. Hazard. Mater.* **2009**, *171*, 393–399. [CrossRef] [PubMed]

13. Genuino, H.C.; Dharmarathna, S.; Njagi, E.C.; Mei, M.C.; Suib, S.L. Gas-Phase Total Oxidation of Benzene, Toluene, Ethylbenzene, and Xylenes Using Shape-Selective Manganese Oxide and Copper Manganese Oxide Catalysts. *J. Phys. Chem. C* **2012**, *116*, 12066–12078. [CrossRef]

14. Leguizamón Aparicio, M.S.; Lick, I.D. Total oxidation of propane and naphthalene from emission sources with supported cobalt catalysts. *React. Kinet. Catal. Lett.* **2016**, *119*, 469–479. [CrossRef]

15. Leguizamón Aparicio, M.S.; Canafoglia, M.E.; Ocsachoque, M.A.; Lick, I.D.; Botto, I.L. Co-Rh modified natural zeolites as new catalytic materials to oxidize propane and naphthalene from emission sources. *Open Chem.* **2016**, *14*, 335–342. [CrossRef]

16. Ojala, S.; Pitkäaho, S.; Laitinen, T.; Koivikko, N.N.; Brahmi, R.; Gaálová, J.; Matejova, L.; Kucherov, A.; Päivärinta, S.; Hirschmann, C.; et al. Catalysis in VOC Abatement. *Top. Catal.* **2011**, *54*, 1224–1256. [CrossRef]

17. Tomatis, M.; Xu, H.-H.; He, J.; Zhang, X.-D. Recent Development of Catalysts for Removal of Volatile Organic Compounds in Flue Gas by Combustion: A Review. *J. Chem.* **2016**, *2016*, 15. [CrossRef]

18. Clarke, T.J.; Kondrat, S.A.; Taylor, S.H. Total oxidation of naphthalene using copper manganese oxide catalysts. *Catal. Today* **2015**, *258*, 610–615. [CrossRef]

19. Wyrwalski, F.; Lamonier, J.-F.; Siffert, S.; Aboukaïs, A. Additional effects of cobalt precursor and zirconia support modifications for the design of efficient VOC oxidation catalysts. *Appl. Catal. B* **2007**, *70*, 393–399. [CrossRef]

20. Pecchi, G.; Reyes, P.; Gómez, R.; López, T.; Fierro, J.L.G. Methane combustion on Rh/ZrO$_2$ catalysts. *Appl. Catal. B Environ.* **1998**, *17*, L7–L13. [CrossRef]

21. Labaki, M.; Siffert, S.; Lamonier, J.-F.; Zhilinskaya, E.A.; Aboukaïs, A. Total oxidation of propene and toluene in the presence ofzirconia doped by copper and yttrium Role of anionic vacancies. *Appl. Catal. B Environ.* **2003**, *43*, 261–271. [CrossRef]

22. Gómez, L.E.; Tiscornia, I.S.; Boix, A.V.; Miró, E.E. Co/ZrO$_2$ catalysts coated on cordierite monoliths for CO preferential oxidation. *Appl. Catal. A* **2011**, *401*, 124–133. [CrossRef]

23. Gutiérrez-Ortiz, J.I.; Rivas, B.D.; López-Fonseca, R.; González-Velasco, J.R. Catalytic purification of waste gases containing VOC mixtures with Ce/Zr solid solutions. *Appl. Catal. B Environ.* **2006**, *65*, 191–200. [CrossRef]

24. De Rivas, B.; Sampedro, C.; García-Real, M.; López-Fonseca, R.; Gutiérrez-Ortiz, J.I. Promoted activity of sulphated Ce/Zr mixed oxides for chlorinated VOC oxidative abatement. *Appl. Catal. B Environ.* **2013**, *129*, 225–235. [CrossRef]

25. Yamaguchi, T. Application of ZrO$_2$ as a catalyst and a catalyst support. *Catal. Today* **1994**, *20*, 199–218. [CrossRef]

26. Ray, J.C.; Saha, C.R.; Pramanik, P. Stabilized nanoparticles of metastable ZrO_2 with Cr^{3+}/Cr^{4+} cations: Preparation from a polymer precursor and the study of the thermal and structural properties. *J. Eur. Ceram. Soc.* **2002**, *22*, 851–862. [CrossRef]

27. Shie, J.-L.; Chang, C.-Y.; Chen, J.-H.; Tsai, W.-T.; Chen, Y.-H.; Chiou, C.-S.; Chang, C.-F. Catalytic oxidation of naphthalene using a Pt/Al_2O_3 catalyst. *Appl. Catal. B Environ.* **2005**, *58*, 289–297. [CrossRef]

28. Ntainjua, N.E.; Carley, A.F.; Taylor, S.H. The role of support on the performance of platinum-based catalysts for the total oxidation of polycyclic aromatic hydro-carbons. *Catal. Today* **2008**, *137*, 362–366. [CrossRef]

29. Zhang, X.-W.; Shen, S.-C.; Yu, L.E.; Kawi, S.; Hidajat, K.; Simon Ng, K.Y. Oxidative decomposition of naphthalene by supported metal catalysts. *Appl. Catal. A Gen.* **2003**, *250*, 341–352. [CrossRef]

30. Garcia, T.; Solsona, B.; Taylor, S.H. Nano-crystalline Ceria Catalysts for the Abatement of Polycyclic Aromatic Hydrocarbons. *Catal. Lett.* **2005**, *105*, 183–189. [CrossRef]

31. Bampenrat, A.; Meeyoo, V.; Kitiyanan, B.; Rangsunvigit, P.; Rirksomboon, T. Catalytic oxidation of naphthalene over CeO_2–ZrO_2 mixed oxide catalysts. *Catal. Commun.* **2008**, *9*, 2349–2352. [CrossRef]

32. Xie, Y.; Tang, Y. Spontaneous monolayer dispersion of oxides and salts onto surfaces of supports: Applications to heterogeneous catalysis. *Adv. Catal.* **1990**, *37*, 1–43.

33. Liu, Z.; Amiridis, M.D.; Yi, C. Characterization of CuO Supported on Tetragonal ZrO_2 Catalysts for N_2O Decomposition to N_2. *J. Phys. Chem. B* **2005**, *109*, 1251–1255. [CrossRef] [PubMed]

34. Rezaei, M.; Alavi, S.M.; Sahebdelfar, S.; Xinmei, L.; Qian, L.; Yan, Z. CO_2-CH_4 Reforming over Nickel Catalysts Supported on Mesoporous Nanocrystalline Zirconia with High Surface Area. *Energy Fuels* **2007**, *21*, 581–589. [CrossRef]

35. Valigi, M.; Gazzoli, D.; Dragone, R.; Gherardi, M.; Minelli, G. Nichel oxide-zirconium oxide: Ni^{2+} incorporation and its influence on the phase transition and sintering of zirconia. *J. Mater. Chem.* **1995**, *5*, 183–189. [CrossRef]

36. Koo, K.Y.; Roh, H.S.; Jung, U.H.; Wang, L.Y. CeO_2 Promoted Ni/Al_2O_3 Catalyst in Combined Steam and Carbon Dioxide Reforming of Methane for Gas to Liquid (GTL) Process. *Catal. Lett.* **2009**, *130*, 217–221. [CrossRef]

37. De Sousa, H.S.A.; da Silva, A.N.; Castro, A.J.R.; Campos, A.; Filho, J.M.; Oliveira, A.C. Mesoporous catalysts for dry reforming of methane: Correlation between structure and deactivation behaviour of Ni-containing catalysts. *Int. J. Hydrogen Energy* **2012**, *37*, 12281–12291. [CrossRef]

38. Liu, Q.; Wang, L.C.; Chen, M.; Cao, Y.; He, H.Y.; Fan, K.N. Dry citrate-precursor synthesized nanocrystalline cobalt oxide as highly active catalyst for total oxidation of propane. *J. Catal.* **2009**, *263*, 104–113. [CrossRef]

39. Trigueiro, F.E.; Ferreira, C.M.; Volta, J.C.; González, W.A.; Pries de Oliveria, P.G. Effect of niobium addition to $Co/\gamma Al_2O_3$ catalyst on methane combustion. *Catal. Today* **2006**, *118*, 425–432. [CrossRef]

40. Solsona, B.; Davies, T.E.; García, T.; Vázquez, I.; Dejoza, A.; Taylor, S.H. Total oxidation of propane using nanocrystalline cobalt oxide and supported cobalt oxide catalysts. *Appl. Catal. B Environ.* **2008**, *84*, 176–184. [CrossRef]

41. Sato, A.G.; Volanti, D.P.; Meira, D.M.; Damyanova, S.; Longo, E.; Bueno, J.M.C. Effect of the ZrO_2 phase on the structure and behavior of supported Cu catalysts for ethanol conversion. *J. Catal.* **2013**, *307*, 1–17. [CrossRef]

42. Kyun Park, B.; Jeong, S.; Kim, D.; Moon, J.; Lim, S.; Kim, J.S. Synthesis and size control of monodisperse copper nanoparticles by polyolmethod. *J. Colloid Interface Sci.* **2007**, *311*, 417–424. [CrossRef] [PubMed]

43. Keramidas, V.G.; White, W.B. Raman Scattering Study of the Crystallization and Phase Transformations of ZrO_2. *J. Am. Ceram. Soc.* **1974**, *57*, 22–24. [CrossRef]

44. Yashima, M.; Ohtake, K.; Kakihana, M.; Arashi, H.; Yoshimura, M. Determination of tetragonal-cubic phase boundary of $Zr_{1-X}R_XO_{2-X2}$ (R = Nd, Sm, Y, Er and Yb) by Raman scattering. *J. Phys. Chem. Solids* **1996**, *57*, 17–24. [CrossRef]

45. Hagjiev, V.G.; Iliev, M.N.; Vergilov, I.V. The Raman spectra of Co_3O_4. *J. Phys. C* **1988**, *21*, L199–L201. [CrossRef]

46. Choi, H.C.; Jung, Y.M.; Noda, I.; Kim, S.B. A Study of the Mechanism of the Electrochemical Reaction of Lithium with CoO by Two-Dimensional Soft X-ray Absorption Spectroscopy (2D XAS), 2D Raman, and 2D Heterospectral XAS−Raman Correlation Analysis. *J. Phys. Chem. B* **2003**, *107*, 5806–5811. [CrossRef]

47. Mironova-Ulmane, N.; Kuzmin, A.; Steins, I.; Grabis, J.; Sildos, I.; Pärs, M. Raman scattering in nanosized nickel oxide NiO. *J. Phys.* **2007**, *93*, 012039–012043. [CrossRef]

48. Wang, W.; Liu, Y.; Xu, C.; Zheng, C.; Wang, G. Synthesis of NiO nanorods by a novel simple precursor thermal decomposition approach. *Chem. Phys. Lett.* **2002**, *362*, 119–122. [CrossRef]

49. Xu, J.F.; Ji, W.; Shen, Z.X.; Li, W.S.; Tang, S.H.; Ye, X.R.; Jia, D.Z.; Xin, X.Q.J. Raman spectra of CuO nanocrystals. *Raman Spectrosc.* **1999**, *30*, 413–415. [CrossRef]

50. Chuah, G.K.; Jaenicke, S. The preparation of high surface area zirconia - Influence of precipitating agent and digestion. *Appl. Catal. A* **1997**, *163*, 261–273. [CrossRef]

51. Song, X.; Sayari, A. Sulfated Zirconia-Based Strong Solid-Acid Catalysts: Recent Progress. *Catal. Rev.* **1996**, *38*, 329–412. [CrossRef]

52. Normair, C.J.; Goulding, P.A.; McAlpine, I. Role of anions in the surface area stabilisation of zirconia. *Catal. Today* **1994**, *20*, 313–321. [CrossRef]

53. Shannon, R.D. Revised Effective Ionic Radii and Systematic Studies of Interatomic Distances in Halides and Chalcogenides. *Acta Crystallogr.* **1976**, *32*, 751–767. [CrossRef]

54. Dow, W.P.; Huang, T.J. Effects of Oxygen Vacancy of Yttria-Stabilized Zirconia Support on Carbon Monoxide Oxidation over Copper Catalyst. *J. Catal.* **1994**, *147*, 322–332. [CrossRef]

55. Kulyova, S.P.; Lunina, E.V.; Lunin, V.V.; Kostyuk, B.G.; Muravyova, G.P.; Kharlanov, A.N.; Jilinskaya, E.; Aboukaïs, A. Redox Behavior of $Y_{0.05}Ce_{0.1}Zr_{0.85}O_2$ and $Y_{0.1}Ce_{0.1}Zr_{0.8}O_2$ System Catalysts Doped with Copper (II). *Chem. Mater.* **2001**, *13*, 1491–1496. [CrossRef]

56. Nanda, B.; Pradhan, A.C.; Parida, K.M. Fabrication of mesoporous CuO/ZrO_2-MCM-41 nanocomposites for photocatalytic reduction of Cr(VI). *Chem. Eng. J.* **2017**, *316*, 1122–1135. [CrossRef]

57. Freitas, I.C.; Damyanova, S.; Oliveira, D.C.; Marques, C.M.P.; Bueno, J.M.C. Effect of Cu content on the surface and catalytic properties of Cu/ZrO_2 catalyst for ethanol dehydrogenation. *J. Mol. Catal. A Chem.* **2014**, *381*, 26–37. [CrossRef]

58. Aguila, G.; Valenzuela, A.; Guerrero, S.; Araya, P. WGS activity of a novel $Cu–ZrO_2$ catalyst prepared by a reflux method. Comparison with a conventional impregnation method. *Catal. Commun.* **2013**, *39*, 82–85. [CrossRef]

59. Baeza, P.; Bassi, R.; Villarroel, M.; Ojeda, J.; Araya, P.; Aguila, G. Adsorption of 4,6-dimethyldibenzothiophene over Cu/ZrO_2. *J. Chil. Chem. Soc.* **2015**, *60*, 2817–2821. [CrossRef]

60. Juan-Juan, J.; Román-Martínez, M.C.; Illán-Gómez, M.J. Nickel catalyst activation in the carbon dioxide reforming of methane: Effect of pretreatments. *Appl. Catal. A Gen.* **2009**, *355*, 27–32. [CrossRef]

61. Tidahy, H.L.; Siffert, S.; Wyrwalski, F.; Lamonier, J.; Aboukais, A. Catalytic activity of copper and palladium based catalysts for toluene total oxidation. *Catal. Today* **2007**, *119*, 317–320. [CrossRef]

62. Fierro, G.; Lojacono, M.; Inversi, M.; Porta, P.; Lavecchia, R.; Cioci, F. A Study of Anomalous Temperature-Programmed Reduction Profiles of Cu_2O, CuO, and CuO-ZnO Catalysts. *J. Catal.* **1994**, *148*, 709–721. [CrossRef]

63. Aissat, A.; Courcot, D.; Cousin, R.; Siffert, S. VOCs removal in the presence of NOx on $Cs–Cu/ZrO_2$ catalysts. *Catal. Today* **2011**, *117*, 120–125. [CrossRef]

64. Centi, G.; Cerrato, G.; D'Angelo, S.; Finardi, U.; Giamello, E.; Morterra, C.; Perathoner, S. Catalytic behavior and nature of active sites in copper-on-zirconia catalysts for the decomposition of N_2O. *Catal. Today* **1996**, *27*, 265–270. [CrossRef]

65. Carno, J.; Berg, M.; Jaras, S. Catalytic abatement of emissions from small-scale combustion of wood A comparison of the catalytic effect in model and real flue gases. *Fuel* **1996**, *75*, 959–965. [CrossRef]

66. Aranda, A.; Agouram, S.; López, J.M.; Mastral, A.M.; Sellick, D.R.; Solsona, B.; Taylor, S.H.; García, T. Oxygen defects: The key parameter controlling the activity and selectivity of mesoporous copper-doped ceria for the total oxidation of naphthalene. *Appl. Catal. B Environ.* **2012**, *127*, 77–88. [CrossRef]

67. Solsona, B.; Sanchis, R.; Dejoz, A.M.; García, T.; Ruiz-Rodríguez, L.; López Nieto, J.M.; Cecilia, J.A.; Rodríguez-Castellón, E. Total Oxidation of Propane Using CeO_2 and $CuO-CeO_2$ Catalysts Prepared Using Templates of Different Nature. *Catalysts* **2017**, *7*, 96. [CrossRef]